Quantitative study of geometric characteristics and formation mechanism of porosity defects in selective laser melted Ti6Al4V alloy by micro-computed tomography

Na-ying AN[1], San-san SHUAI[1], Chao-yue CHEN[1], Li-ming LEI[2], Jiang WANG[1], Zhong-ming REN[1]

1. State Key Laboratory of Advanced Special Steels, School of Materials Science and Engineering,
Shanghai University, Shanghai 200444, China;
2. AECC Shanghai Commercial Aircraft Engine Manufacturing Co., Ltd., Shanghai 201306, China

Abstract: The defects formed inside the additive manufactured (AM) part have a detrimental effect on the mechanical performance of the printed component. The effect of defects on the performance of parts varies with their geometry features. The characteristics of porosity defects in 36 bulk Ti6Al4V specimens with different printing parameters were investigated via X-ray computed tomography (XCT). The porosity defects are classified into four types: spherical-shaped, elliptical-shaped, elongated-shaped and irregularly-shaped pores, based on their geometric characteristics. Elongated-shaped defects account for the largest proportion of defects with all printing parameters, and the proportion of irregularly-shaped defects enhances with the increase of scanning speed. The characteristics of gradual accumulation of defects in single-track and multi-track samples were also analyzed. Porosity may gradually accumulate with the overlay of layers, while the appropriate overlapping rate may melt the pores between the tracks. The formation of defects is greatly influenced by surface roughness and pool wetting.

Key words: selective laser melting; X-ray computed tomography; porosity defect; 3D geometric morphology; formation mechanism; Ti6Al4V alloy

1 Introduction

Selective laser melting (SLM) is one of the most mature processes in metal additive manufacturing (AM) based on layer-by-layer fabrication. Due to the characteristics of fast speed, and small spot diameter [1], SLM enables to produce complex-geometry components with design flexibility, high performance, and multi-functionalization. Till now, SLM has been applied in aerospace, biomedicine [2], and other fields. Its forming materials include stainless steel [3], titanium alloy [4,5], magnesium alloy [6,7], and superalloy [8].

However, a series of complex non-equilibrium physical and chemical metallurgical behaviors will occur during SLM [9], and the unstable molten pool will inevitably cause defects in samples [10]. Defects in SLM generally include pores [11], unfused power defects [12,13], balling, spatters [14] and cracks [15], etc. The defect characteristics are dependent on the processing parameters [16−18], which have different effects on the mechanical properties [19−22]. In order to characterize these defects [23], the advantages of computed tomography (CT) technology in the non-destructive test of complex parts and defect detection are becoming more prominent [24,25]. This technique can provide the internal structure of materials and the three-

dimensional (3D) visualization of defects [26,27].

Based on this technique, some researchers have paid attention to the influence of processing parameters on the 3D defects. ELAMBASSERIL et al [28] compared the defect characteristics of cylindrical rods by means of X-ray micro computed-tomography (XCT). They found that there was a strong correlation between the characteristics of lack of fusion (LOF) defects and construction height. Similarly, the distribution of defects in metal AM samples and the correlation between defect characteristics were explored by SANAEI et al [29]. STEF et al [30] used XCT to show that LOF defects caused by the low energy around the laser spot is the main mechanism of pore formation.

In order to deeply study the formation mechanism of defects in SLM, the defect formed in a single track or layer was investigated [31,32]. XIANG et al [33] used XCT to study the effect of linear energy density (LED) on the single-track porosity of Inconel 625 alloy. The results showed that the porosity increased with increasing LED in the keyhole mode. Furthermore, SHRESTHA et al [34] characterized the pore defects formed during the single track of SLM via XCT, showing that the laser power has a greater influence on the pore number and volume than the scanning speed. However, there is no uniform conclusion on the quantitative and qualitative relationship between the 3D morphology of defects and processing parameters. The better application of XCT to characterize the gradual accumulation of single-track and multi-track defects during SLM is of great significance for better understanding their formation mechanism [35,36].

In this study, high-resolution XCT and scanning electron microscope (SEM) were used to characterize the defect characteristic information in the samples. Single-track, multi-track, and bulk samples were prepared with different processing parameters. The evolution of defects under different processing parameters during SLM was obtained. Following this, the mechanism of defect formation was also discussed based on melt viscosity, melt flow, surface tension, and temperature gradient.

2 Experimental

2.1 Materials and additive manufacturing

The powder used in the study was the gas atomized Ti6Al4V (Ti−6wt.%Al−4wt.%V) alloy produced by Bright Laser Technologies. The composition of the main chemical elements measured by ICP is given in Table 1. 3D images obtained by CT in Fig. 1(a) show that Ti6Al4V powders have a spherical morphology. The laser diffraction size analyzer (Mastersizer 2000, Malvern Instruments, UK) was also used to characterize Ti6Al4V powder, and its particle size distribution was $D_{10}=17.67$ μm, $D_{50}=35.10$ μm, and $D_{90}=58.07$ μm. Figure 1(b) compares the particle size volume fraction results using a laser analyzer and CT.

The SLM equipment used in this study was Prox−200 from 3D systems, which utilized the fiber laser with a spot diameter of 75 μm. The maximum power of the laser was 300 W, and the maximum

Table 1 Chemical composition of Ti6Al4V powder (wt.%)

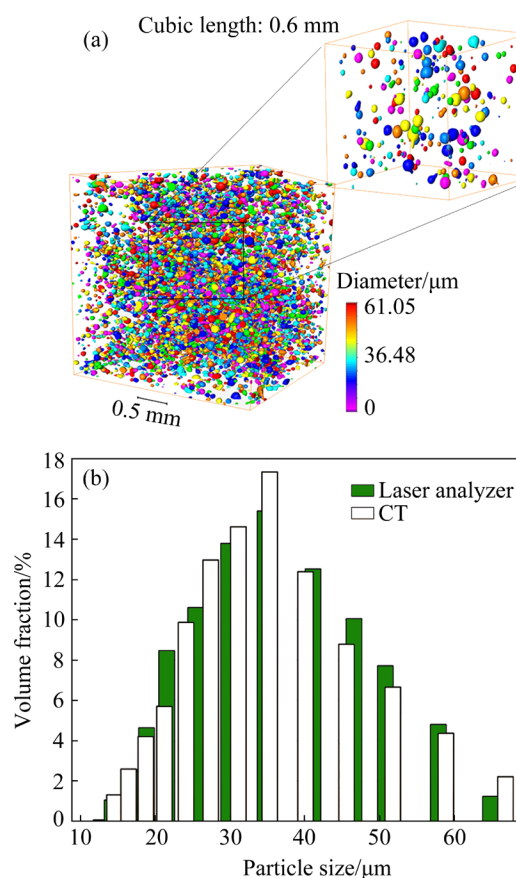| C	O	N	H	Al	V	Fe	Ti
0.007	0.085	0.05	0.003	5.95	3.72	0.15	Bal.

Fig. 1 Characteristics of Ti6Al4V powder: (a) CT analysis; (b) Particle size distribution measured by laser analyzer and CT

scanning speed was 5000 mm/s. During SLM processing, argon with a purity of 99% was used as the protective gas to ensure that the oxygen content was below 5×10^{-2} wt.%, minimizing the oxidation of metal materials under the high-temperature conditions.

2.2 Methods

Before the experiment, the powder was preheated for 6 h in the vacuum oven at 80 °C to prevent residual moisture in the powder from causing too many defects in the parts. The processing parameters of cubic samples selected in the experiment are listed in Table 2, with laser power P and scanning speed V as variables, and the powder thickness for each layer was 30 μm. Cubic samples with dimensions of 4 mm × 4 mm × 5 mm were printed on 126 mm × 126 mm × 5 mm substrate using SLM technique. The scanning direction was rotated by 90° for each layer scanned by the laser, and the samples were formed on the z-axis. Thereafter, the samples were cut from the substrate and numbered consecutively for further characterization.

Table 2 Processing parameters of cubic samples

Processing parameter	Value
Laser power/W	120, 150, 180, 210, 240, 270
Scanning speed/ (mm·s^{-1})	800, 1000, 1200, 1400, 1600, 1800

In order to reveal the formation mechanism of the gradual accumulation of porosity defects in the processing of SLM, the single-track single-layer, multi-track single-layer and multi-track multi-layer samples were also studied and characterized following the bulk sample experiment. As given in Table 3, these laser processing parameters were chosen when preparing the single-track single-layer, and multi-track multi-layer samples. Closely packed tracks with varying hatch spacings from 40 to 80 μm were scanned to generate several multi-track samples. All the single and multi-track samples were 8 mm in length and deposited using only one scanning vector for each layer. Macroscopic appearances and molten pool characteristics of the single tracks were observed using SEM (FEI Nova Nano SEM 450) and LOM (Light optical microscope, OLYMPUSDP71).

Table 3 Processing parameters of single and multi-track samples

Processing parameter	Value
Laser power/W	150, 180, 210
Scanning speed/ (mm·s^{-1})	800, 1000, 1200, 1400, 1600, 1800
Number of tracks	2, 4, 6, 8
Number of layers	2, 4, 6, 8

2.3 XCT characterization

The micro-CT equipment in this work was provided by North Star Imaging (NSI) Company. The equipment is composed of three parts: a 225 kV X-ray source with a minimum focal spot size of ~2 μm, a sample table, and a Perkin Elmer flat panel detector (2048 × 2048 pixels in 16-bit depth image). During the measurement, the sample was irradiated with a cone beam of X-ray. When the sample rotated over 360°, 1440 projected images (step length of 0.25) were obtained with an exposure time of 1000 ms at each position. In this experiment, XCT was performed using a target current of 30 μA and an accelerating voltage of 120 kV. Then, the projections were reconstructed via efX-CT software with ring reduction and beam hardening correction. The final voxel size of the 3D images was 2.3 μm × 2.3 μm × 2.3 μm. The reconstructed slices were imported into Avizo 9 software (Thermofisher, USA) for qualitative and quantitative analysis as well as 3D rendering, and then the volume, size, spatial distribution and geometry morphology of porosity defects were obtained by statistical analysis [37].

3 Results

3.1 3D characterization of defects in cubic samples via XCT

3.1.1 Porosity and morphology characteristics

In the processing of SLM, the complex physical phenomena such as powder melting and pool wetting were mainly dominated by heat transfer. Energy transfer affected the fusion level and solidification rate of metal powder and the input energy directly or indirectly affected the formation of pores, balling, cracks, and other defects in the AM parts. Many researchers introduced the energy density (D_E, J/mm^3) as a processing variant [38], which includes several

significant processing parameters as defined in Eq. (1):

$$D_{\mathrm{E}} = \frac{P}{v \cdot h \cdot t} \qquad (1)$$

where P is laser power (W), v is scan speed (mm/s), h is hatch spacing (mm) and t is layer thickness (mm).

Under certain hatch spacing and layer thickness, the combination of different laser power and scanning speed can produce different energy density. Figure 2 shows the defect morphology characterized by XCT of SLM-manufactured Ti6Al4V cubic samples with different laser powers and scanning speeds in this work. The image can be divided into three regions: keyhole defect zone, optimal parameter zone and LOF defect zone, based on the number and geometry features of the pores. There are seven parameters of XCT pore characterization in these three regions. A1, A2, and B1 samples were formed under the parameters of high power (>210 W) and low scanning speed (<1200 mm/s). The energy density input on the powder bed is larger at this time, and the solubility of the gas in the molten pool is higher. Further, with the cooling of the molten pool, the solubility of gas decreases, which increases the possibility of gas residue. Thus, it is easy to form keyhole defects whose 3D morphology is usually spherical and less than 100 μm in size.

However, in the area of low laser power (<180 W) and high scanning speed (>1200 mm/s), due to the lack of input energy, the incomplete melting of the powder leads to the formation of LOF defects. LOF defects are a common type of defect in Ti6Al4V manufactured by SLM. They are often associated with unmelted powder particles and pores formed by insufficient melting, mainly in the form of irregular strip or open area defects, and sometimes intermittent spots. The lack of energy input in the processing of SLM and the lack of laps in the molten metal can give rise to this kind of defect, which has a great influence on the mechanical properties of the AM parts [39,40].

As shown in B2, D1 and E1 samples in Fig. 2, LOF defects are usually large and perpendicular to the z direction (construction direction) of the AM part. In the place where the LOF defects have been formed, with the subsequent deposition processing, the surface quality of the defects is poor, which makes the defects gradually expand upward and ultimately a larger layer defect is formed. Table 4 gives different processing parameters and pore information via XCT of seven Ti6Al4V samples manufactured by SLM. Sample C1 has the lowest number of pores and the highest density (99.92%) among all the samples. As the energy density decreases gradually, the porosity of the sample decreases at first (such as A1, A2, and B1 samples) and then increases (such as C1, D1, and E1 samples).

3.1.2 Pore orientation and surface curvature

Since the SLM is a layer-by-layer forming process, the change in orientation of internal pores in Ti6Al4V samples is associated with the z direction [41]. Figure 3(a) displays a unit ball with a radius of 1, where θ [−180°, 180°] and φ [0°, 90°] are two angles that describe vector $\boldsymbol{r}$. φ represents
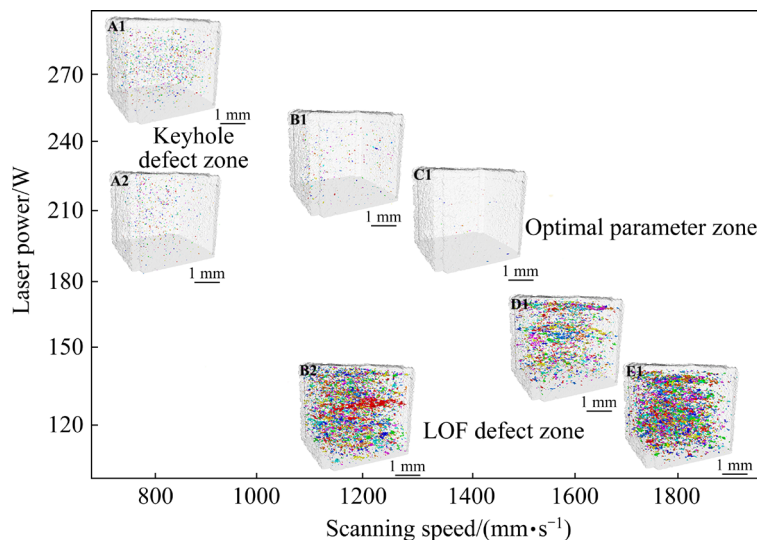

Fig. 2 Defect morphology of SLM Ti6Al4V cubic samples with different laser powers and scanning speeds

Table 4 Processing parameters and pore information by XCT of SLM Ti6Al4V samples

Sample	Laser power/ W	Scanning speed/ (mm·s^{-1})	Energy density/ (J·mm^{-3})	Pore count	Porosity/ %
A1	270	800	132.4	3828	0.68
A2	210	800	120.9	2780	0.32
B1	240	1200	78.4	1426	0.23
C1	210	1400	58.8	17	0.08
B2	120	1200	39.2	9013	2.75
D1	150	1600	36.8	7176	1.5
E1	120	1800	26.1	15031	5.07
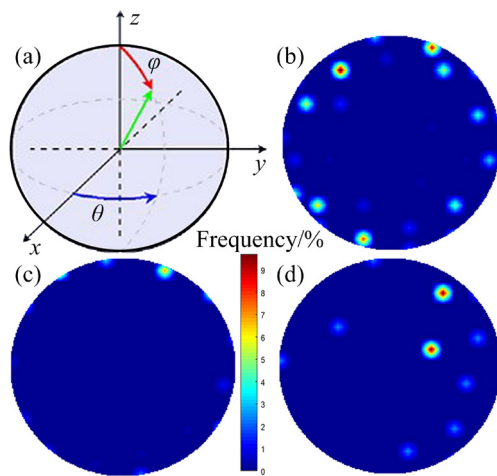
Fig. 3 Azimuthal and polar angles (a) and orientation contour plots of all internal pores in SLM-manufactured Ti6Al4V samples with P=120 W, v=1800 mm/s (b), P= 210 W, v=1400 mm/s (c) and P=270 W, v=1200 mm/s (d)

the angle between vector r and z-axis. The end of vector r is on the sphere. The long axis of all pores can be regarded as vectors, and all the vectors in each sample are projected on the xoy. Thereafter the orientation contour plot is obtained (Fig. 3). Each bright spot represents the position of orientation, and when the pore orientation is at the origin position, it means that the direction of the pore is parallel to the z-axis. Moreover, the orientations with high frequency are shown in red and the lower ones are in blue. When laser power is 120 W and the scanning speed is 1800 mm/s (Fig. 3(b)), the highest concentrations are found close to the edge of the image, illustrating that internal pores are mostly oriented perpendicular to the construction direction, indicating the LOF defects. Figure 3(c) shows a small number of LOF defects at P=210 W, and v=1400 mm/s. When the laser power is 270 W

and the scanning speed is 1200 mm/s (Fig. 3(d)), the highest concentrations are found between the origin and the circumference, which shows that most of the pores are inclined, not parallel or vertical. The above analysis proves that the orientation of pores is also related to the selection of processing parameters, and the XCT characterization of pores in a 3D direction is more convincing than 2D metallographic analysis.

Surface curvature can quantitatively describe the 3D characteristics of the defects, and the curvature of defects affects the mechanical properties of the AM part, such as crack formation and propagation [42]. The data from XCT were reconstructed and created as voxel-based surfaces for porosity defects inside the samples. The entire surface was replaced by a triangular approximation. Then, the curvature value of the two directly adjacent triangles on the surface was calculated, and the initial curvature value was averaged four times with the curvature value of the directly adjacent triangle. Thus, the smooth initial curvature value was obtained. Each surface can be represented by two principal curvature values k_1 and k_2 [43], from which the mean curvature (H) and the Gaussian curvature (K) are obtained as follows:

$$H=1/2(k_1+k_2) \tag{2}$$
$$K=k_1k_2 \tag{3}$$

Figure 4(a) shows the interfacial shape distribution (ISD) based on the principal curvature distribution (k_1, k_2). ISD is realized by using the contour plots generated by 3D probability plots. The map shows different interface areas and corresponding shapes. We can get the following specific information:

(1) The curvature on the line $k_1=k_2$ indicates that the pore surface has spherical interfacial shapes, which can be convex (H>0) or concave (H<0).

(2) When the curvature is at $k_1=0$ (k_2>0), the pores have cylindrical shapes.

(3) Curvatures with k_1>0 and k_2>0 are defined as upward convex pore surfaces (corresponding to Area 1).

(4) Curvatures with k_1<0 and k_2>0 are defined as saddle-shaped (corresponding to Areas 2 and 3).

(5) Curvatures with k_1<0 and k_2>0 are defined as downward concave surfaces (corresponding to Area 4).
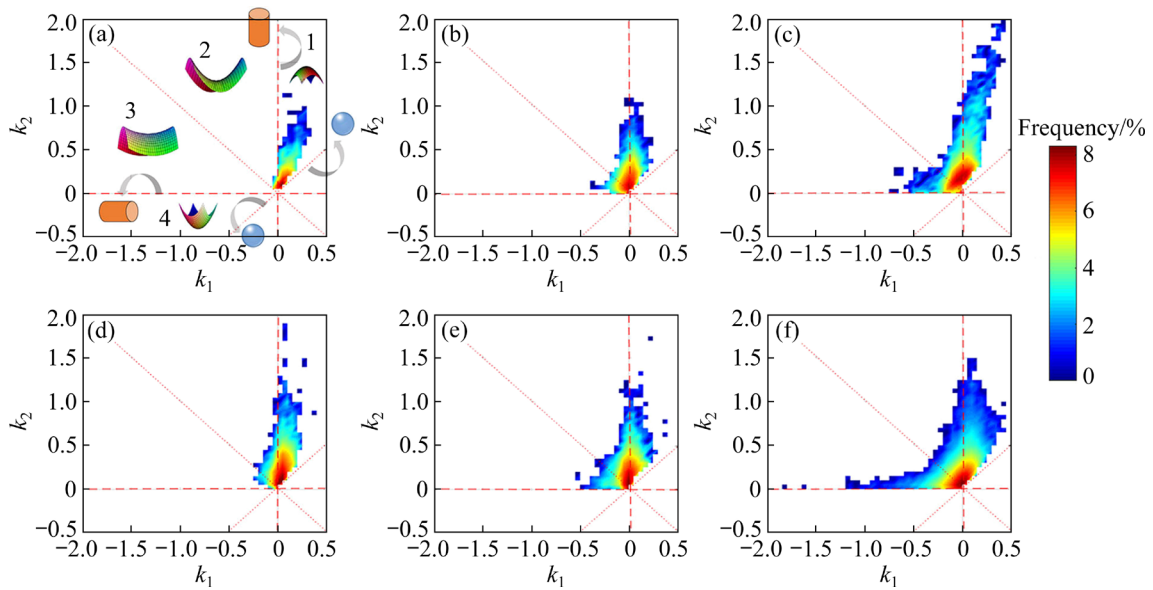
Fig. 4 ISDs of all pores in Ti6Al4V samples by SLM under different processing parameters: (a) P=210 W, v=1200 mm/s; (b) P=240 W, v=1200 mm/s; (c) P=270 W, v=1200 mm/s; (d) P=150 W, v=1000 mm/s; (e) P=150 W, v=1200 mm/s; (f) P=150 W, v=1400 mm/s

(6) Curvatures with k_1=k_2=0 are flat planes.

The principal curvatures can be used to analyze the morphology of porosity defects, as shown in Figs. 4(a−f). These ISDs represent the curvatures of all the pores in Ti6Al4V samples by SLM with different processing parameters. Figures 4(a−c) show the variation of the principal curvature distribution with the increase of laser power (P=210, 240, and 270 W) when the scanning speed is constant (v=1200 mm/s). The blue peak of the ISDs increases continuously upwards, and the area where the principal curvature lies is $k_1 \geq 0$ and $k_2 > 0$. This proves that the energy input increases gradually, and the trend of convex ellipse or global sphere becomes more prominent. This kind of pores shape corresponds to the keyhole defect zone in Fig. 2 at this time. When the laser power is fixed (P=150 W) and the scanning speed increases gradually (v=1000, 1200, and 1400 mm/s), the position of principal curvature changes from k_1=0, $k_2 > 0$ to $k_1 < 0$, $k_2 \geq 0$ (Figs. 4(d−f)). Because of the low energy density, most of the LOF defects are distributed between the layers, and the characteristics of pores gradually change from cylindrical to saddle-shaped. As a result, taking curvature as a quantitative parameter to characterize the relationship between pores and processing parameters can lay a foundation to explore the proportion of defects under the same processing condition.

3.1.3 Classification of 3D defect characteristics

The quantitative morphology information of Ti6Al4V defects, such as diameter, volume, sphericity, and aspect ratio, can be obtained by XCT characterization. Among all the morphology information, the sphericity is an important factor to evaluate the irregularity of the 3D morphology of defects. It ranges from 0 to 1, where the value of 1 indicates a perfect sphere, and the value close to 0 means an extremely irregular defect.

The relative frequencies of the sphericity characteristics of all defects under different laser powers are obtained, as shown in Fig. 5. The peak of each fitting curve represents the defect characteristics with the highest frequency in the sample. At the same laser power, it is found that the range of pore sphericity distributes from 0.2 to 1.0. With the increase of energy density, the peak of all fitting lines moves to the right gradually. Namely, more defects with sphericity approaching unity present as the energy density increases. This proved that the energy input significantly affects the morphology of the defects inside the printed samples. With the increase of energy input, the powder melts completely, thus irregular and non-spherical pores are reduced, and most of the defects are small pores with spherical structures. As shown in Figs. 5(c−e), when the scanning speed is 1000 mm/s, the relative frequency of pores reaches 0.5, which reflects that the high energy input leads
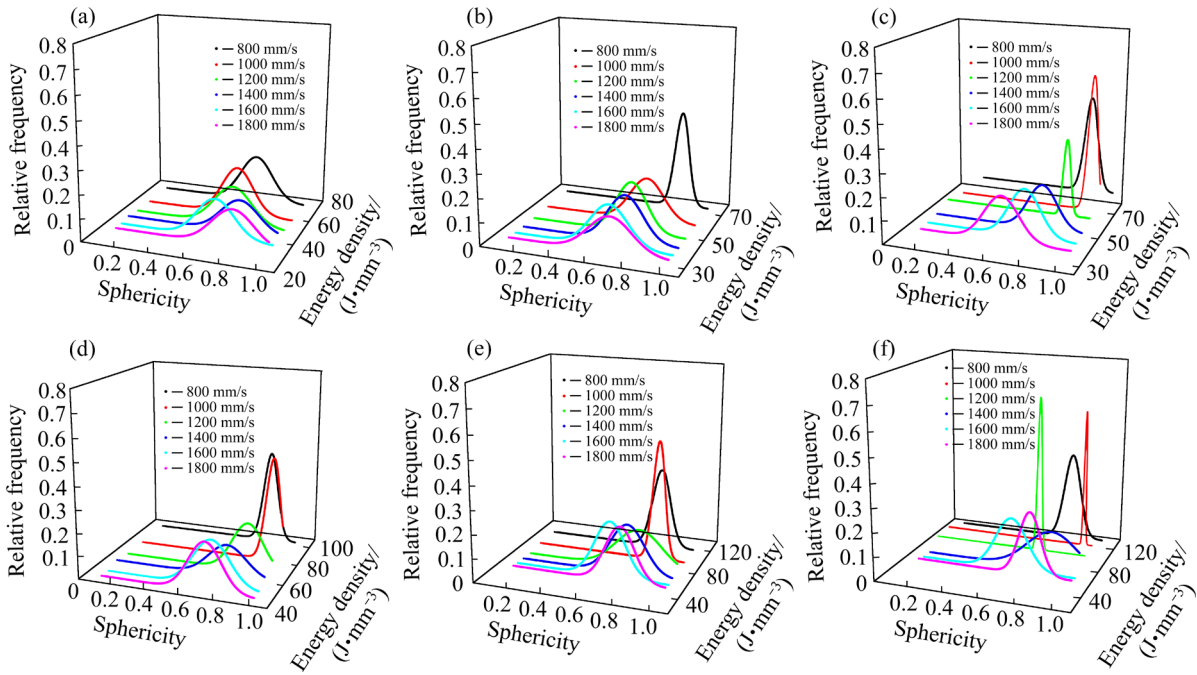
Fig. 5 Relative frequency of defect sphericity with different laser powers: (a) P=120 W; (b) P=150 W; (c) P=180 W; (d) P=210 W; (e) P=240 W; (f) P=270 W

to fewer defects in the sample, so the proportion of nearly spherical pores reaches the highest point (the red line).

Nearly spherical and irregularly shaped defects are not enough to fully summarize all the defect characteristics in Ti6Al4V samples, so it is significant to classify the 3D characteristics of pores by using the defect quantitative information characterized by XCT [44,45]. According to the degree of sphericity, the 3D defect characteristics of Ti6Al4V samples are divided into four types: (1) perfect spherical shape with the sphericity of 0.9−1; (2) elliptical-shaped pores with spherical of 0.7−0.9; (3) elongated-shaped defects with spherical of 0.4−0.7; (4) irregularly-shaped defects with spherical of 0−0.4. Figure 6 shows the visual characterization of four types of defects in Ti6Al4V samples with aspect ratio and sphericity obtained by XCT. The aspect ratio represents the measure of the extension of each defect, with high values representing elongated defects. As illustrated in Fig. 6, along the path of the red arrow, the feature of the defect gradually evolves from the standard sphere to an irregular shape, and the corresponding sphericity decreases as the aspect ratio increases. It is worth noting that when both sphericity and the aspect ratio are low, the defect is still characterized by an irregular shape. This proves that taking the
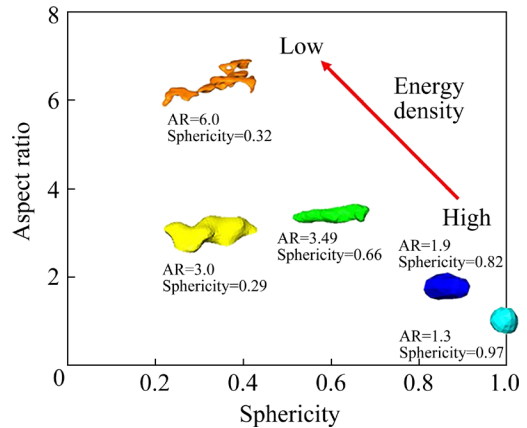

Fig. 6 Visual characterization of four types of defects in Ti6Al4V samples with aspect ratio (AR) and sphericity obtained by XCT

aspect ratio and sphericity into account can more accurately characterize the type of defects in SLM Ti6Al4V, which is beneficial to better understanding their formation mechanism.

The percentage changes of four types of defects under different power inputs are explored (Figs. 7(a−f)). It is observed that elliptical defects account for the highest proportion of almost all parameters, followed by elongated defects. A general trend is that the proportion of irregular defects grows with the increase of scanning speed, but the overall proportion is low, which means that
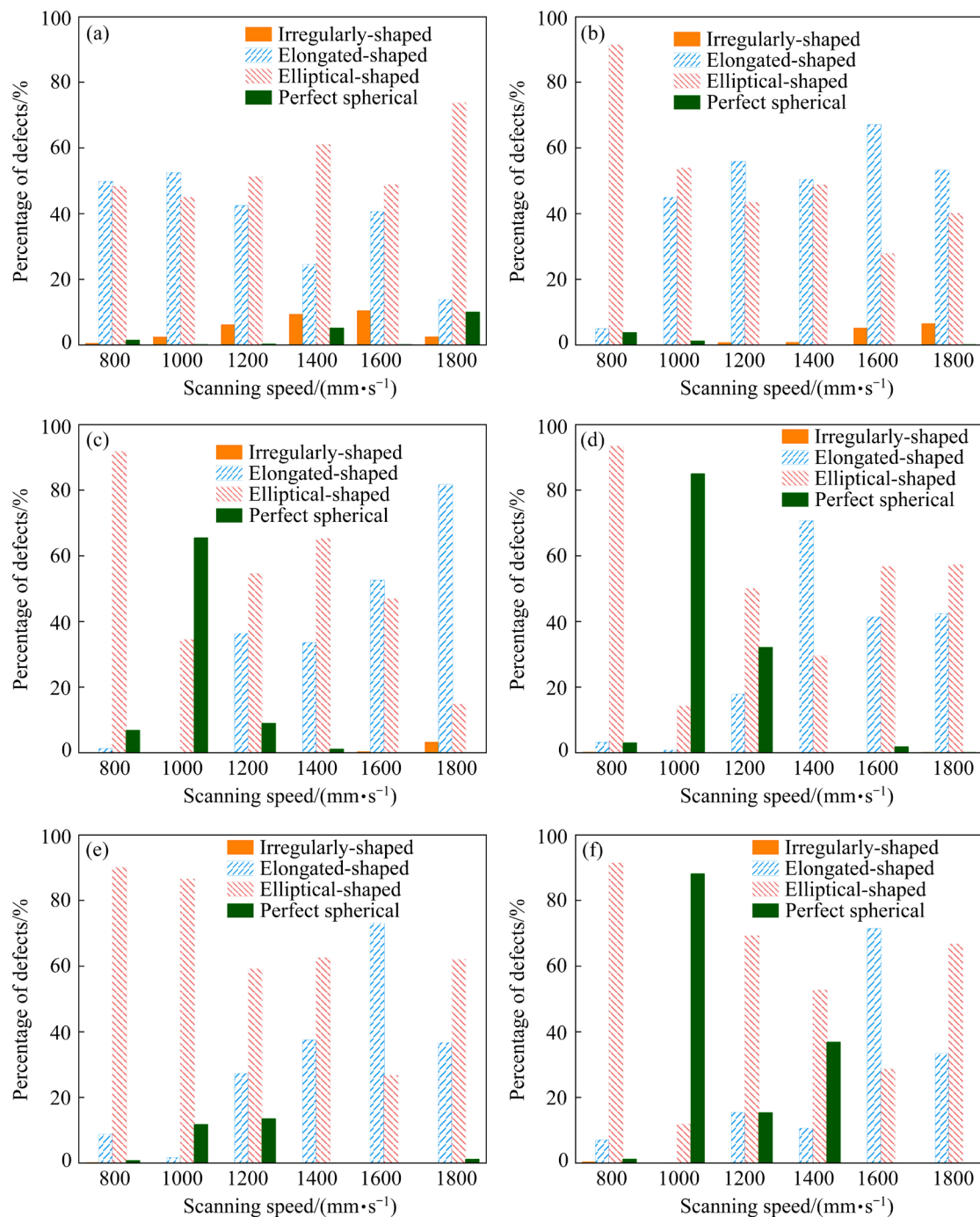
Fig. 7 Percentage of four types of defects with different laser powers: (a) P=120 W; (b) P=150 W; (c) P=180 W; (d) P=210 W; (e) P=240 W; (f) P=270 W

when appropriate laser power and scanning speed are selected, the probability of irregular defects is minimal. The above results indicate that the statistical analyses of the percentages of the four defect features can quantitatively and intuitively show the main characteristic of defects in the sample. Although most of the defects are randomly generated, the present result obtained by XCT might be helpful for future machine learning methods to reveal the changing rules of defect

morphology on the basis of a large number of samples [46].

3.2 3D characterization of surface morphology and defects analysis in layer-by-layer samples via XCT

3.2.1 Single-track single-layer samples

In the processing of SLM, the smallest processing unit is a single track. Understanding the characteristics and defects of a single track helps us

better analyze multi-track multi-layer samples [47]. In order to further study defect characteristics and its formation mechanism, three representative laser power parameters (P=150, 180, and 210 W) were selected for the study of single-track and single-layer sample. Figure 8 shows the SEM surface morphologies of the Ti6Al4V single track with different processing parameters. The morphologies can be roughly divided into two types: stable continuous type (Zone I) and unstable continuous type (Zone II). Zone I is continuous in the morphology, and splash particles with a diameter of about 20−40 μm are found to be attached to the substrate during powder melting. In the processing of SLM, the powder particles absorb the laser energy and release a large amount of surface energy, and the viscosity of the metal liquid phase decreases with the increase of the liquid temperature of the molten pool. The lower the viscosity is, the higher the fluidity and wettability of the melt are. Then, the melt diffuses uniformly to form a smooth and continuous single track.

However, Zone II cannot be stable due to the oscillation of the molten pool. Low power input affects the fluid dynamics of the molten pool and reduces the surface free energy of the metal liquid, thus splitting metal liquid into small droplets to form spheroids. There are many spheroidization and bonding phenomena of unmelted powder on both sides of the single tracks with all these processing parameters. For the same laser power, the width of single tracks is observed to decrease gradually as the scanning speed increases. This phenomenon is attributed to Marangoni convection, which is driven by surface tension gradient. The formation of this kind of convection in the molten pool often changes the strength of the convection in the hot capillary tube, which leads to the instability of liquid [48]. When the energy is insufficient to melt substrate, the surface tension decreases, and the molten metal flows radially outward, resulting in a wider molten pool. In summary, it can be noted that viscosity and Marangoni convection play significant roles in determining melting pool morphology.
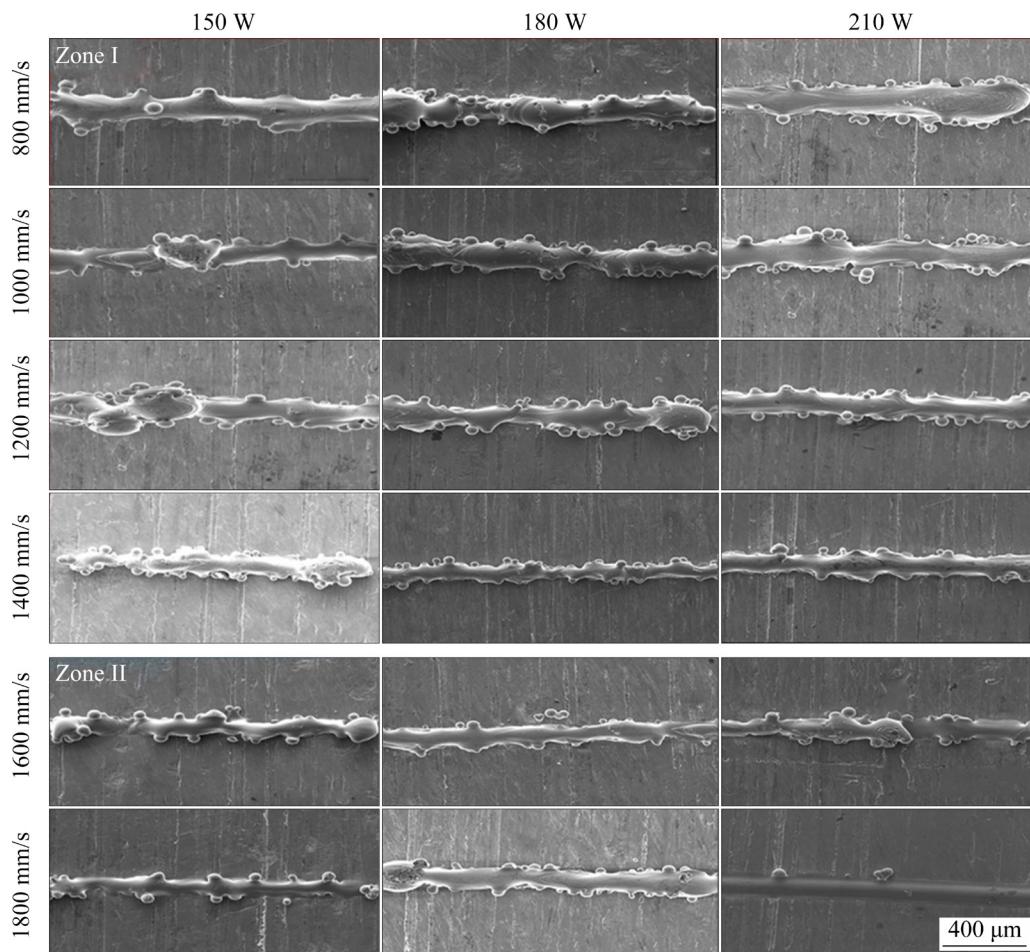

Fig. 8 SEM micrographs of top surface of Ti6Al4V single tracks manufactured by SLM with different processing parameters

In order to further characterize the defects in single tracks, segmentation with local gray value thresholds is applied for 2D sections. 3D visualizations of Ti6Al4V single track morphology and the defects with three different processing parameters are shown in Fig. 9(a). For 210 W laser power and 1000 mm/s scanning speed, the energy density of the single track is higher, and most of the pores are inside the single track, which are small in volume and uniformly distributed. With the decrease of energy density, the number of defects decreases gradually, and there are no obvious pores in the single track. Under this condition, the single-track surface is smooth and continuous. However, for P=150 W and v=1400 mm/s, the single track is not continuous enough, resulting in a very rough surface. Most of the pores are opening defects that irregularly distribute on both sides of the single track.
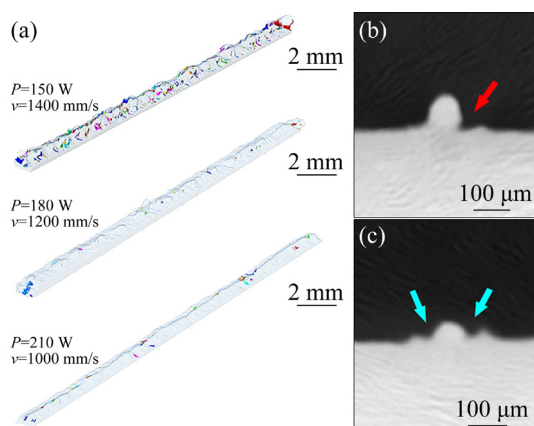

Fig. 9 3D visualizations of Ti6Al4V defects via XCT (a); Typical defects in single-track SLM Ti6Al4V samples (P=210 W, v=1200 mm/s) (b, c) ((b) Cavities at edges on one side; (c) Cavities at edges on both sides)

Figures 9(b, c) show typical defects in the single-track SLM Ti6Al4V samples. Cavities at the edges of the single tracks are shown in 2D slices. The red arrow points to sunken defects on one side of the single track for 210 W and 1200 mm/s, and the blue one represents those on both sides. Laser energy is very high at this time, the internal temperature of the molten pool gradually increases, and the molten metal liquid spreads faster from the center to both sides of the molten pool. Then, the rapid solidification processing causes a depression around the center of the molten pool, which is similar to "W" shape.

3.2.2 Multi-track single-layer samples

In order to further reveal the effect of single-track defects on the quality of SLM parts in three regions in Fig. 2, multi-track single-layer samples with three parameters (P=150 W, v=1600 mm/s; P=180 W, v=1200 mm/s; P=210 W, v=800 mm/s) were chosen. Figure 10 shows the single-layer specimens composed of various numbers of single tracks and pore morphology with 30% and 50% overlapping rates. As the number of single tracks increases, due to the overlap between tracks in the multi-track sample, the formed inter- track defects disappear and the multi-track surface becomes flat and smooth [49]. However, the fluctuation on both sides of the multi-track surface is intenser. The obvious fluctuation of the edge results in the formation of protrusions and depressions on the track, which provides the possibility for the LOF defects of the bulk specimens. In addition, a large number of spatters and unmelted powders can also be observed on the surface of the Ti6Al4V single-layer samples, as displayed in Fig. 10(a). The diameter of the spatters is about 90 μm, which is larger than the size of the unmelted powders (15−53 μm). With the gradual melting of the metal powder and the rising temperature of the molten pool, metal evaporates in the process of laser scanning, which may lead to the instantaneous expansion of the volume through the conversion from solid to gas, thus exerting recoil pressure on the molten pool. When the metal recoil pressure overcomes the surface tension of the molten pool, spatter and depression are formed. Moreover, for 180 W laser power and 1200 mm/s scanning speed (Fig. 10(b)), there are many spherical particles on the upper surface of 4-track samples. The uniformity and continuity of the melting pool are completely destroyed by balling defects. The droplets tend to agglomerate due to the minimum Gibbs surface free energy under the action of surface tension, which leads to the formation of balling easily.

The hatch space describes the distance between the centers of two tracks [50]. The relationship between the overlapping rate and the hatch space is defined as follows:

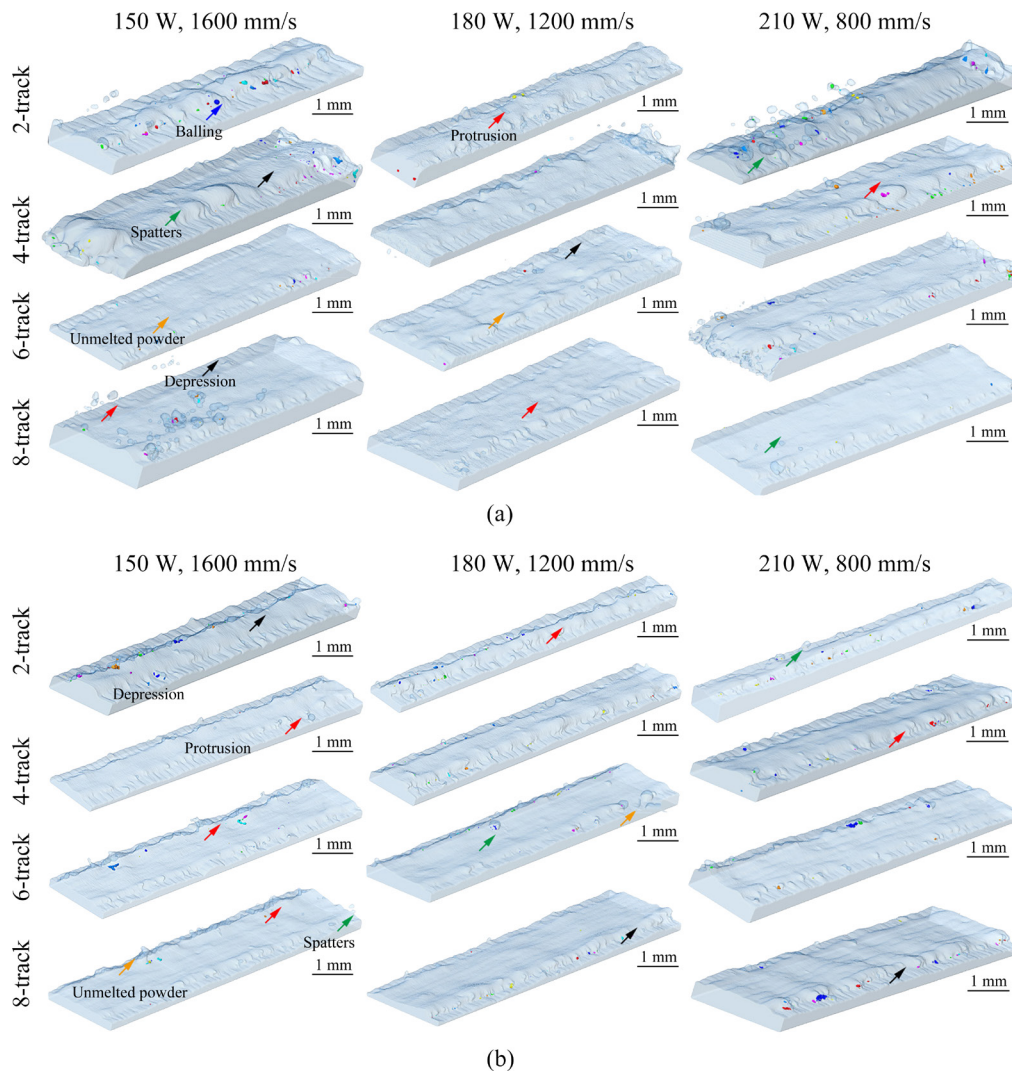$$\psi = \frac{d_\mathrm{m} - s}{d_\mathrm{m}} \times 100\% \tag{4}$$

Fig. 10 Ti6Al4V single-layer samples morphology and pore characteristics with 2, 4, 6, and 8 tracks via XCT at three different processing parameters with 30% (a) and 50% (b) overlapping rates

where ψ represents the overlapping rate, s represents the hatch space, and d_m represents the width of the single-track.

Different overlapping rates affect the surface quality and internal defects of multi-tracks. By comparing the 30% overlapping rate with 50%, it can be detected that the surface of the molten pool is smoother when the overlapping rate is 50%. The reason is partially due to the hatch space being relatively small at this time (50−80 μm), which is close to the focused spot size of 75 μm. In the processing of multi-track, this can ensure uniform energy distribution and full remelting of the molten pool, reducing defects such as warping and deformation caused by poor overlapping. Additionally, with 30% overlapping rate, it is found that the fast solidification rate of liquid metal leads

to the unevenness of the overlapping between the melts, and a large number of pits appear on the surface of the melts. This is because the size of the formed molten pool becomes smaller, and the contact area between the molten pool and the matrix is limited, which is not conducive to the wettability and the fluidity of the molten pool, resulting in long and narrow pores in the tracks.

The number and average equivalent diameter of SLM Ti6Al4V multi-track pores are shown in Fig. 11. The pores contain LOF formed by single-track depressions and gas porosity inside the tracks. In general, the number of pores accumulates gradually with the number of tracks among the three processing parameters. However, the number of pores in the sample with a 50% overlapping rate and 8-track becomes less. This is because the high
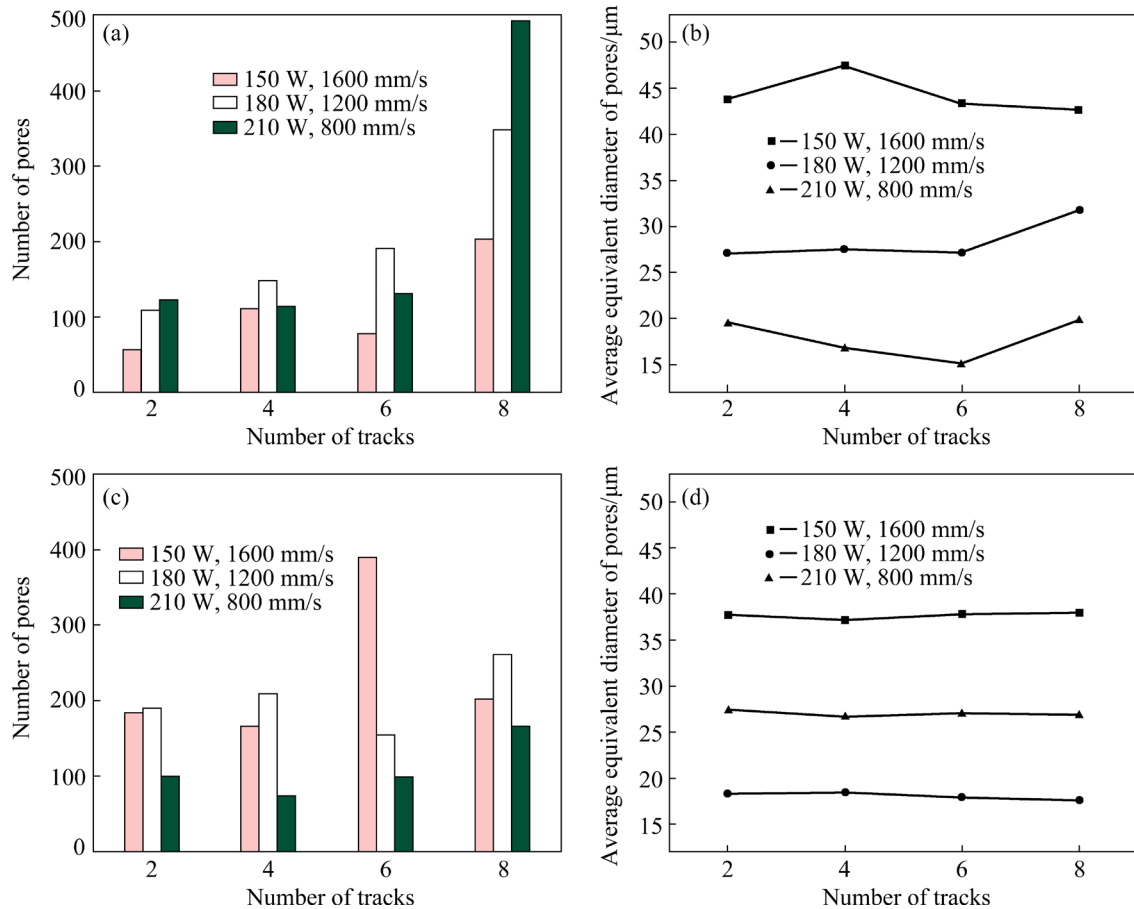
Fig. 11 Number (a, c) and average equivalent diameter (b, d) of SLM Ti6Al4V multi-track pores with 30% (a, b) and 50% (c, d) overlapping rate

power and proper overlapping rate lead to a high remelting rate, which can eliminate some of the formed defects to a certain extent. Besides, the change in the average diameter of pores indicates that the pore size does not enhance with the increase of the number of tracks, but fluctuates in a range. And the fluctuation range of pore diameter of 30% overlapping rate is greater than that of 50%. Hence, the overlapping rate has a great influence on the porosity and the surface quality of Ti6Al4V multi-track samples.

Figure 12(a) shows the typical irregularity pores morphology of 6-track in 3D views by CT when the laser power is 150 W and scanning speed is 1600 mm/s. The pores perpendicular and parallel to the scanning direction can be identified in Fig. 12(b). When the laser power is not high enough for single-track sample powders to melt completely, depressions are formed on both sides, as well as the neighboring single-track, so that the depressions between multiple tracks cause pores perpendicular to the multi-track samples. Besides, it is also found
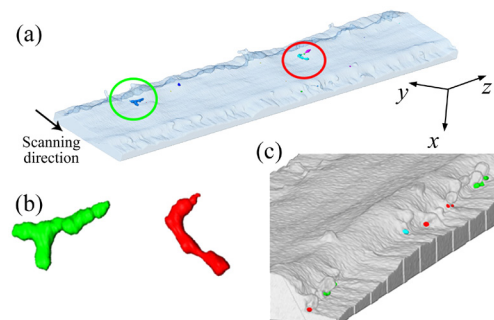

Fig. 12 Irregularity pores morphology of 6-track samples in 3D views by CT at 150 W laser power and 1600 mm/s scanning speed (a); Pore perpendicular/parallel to scanning direction (b); 3D rendering and spherical pores of 6-track samples at 210 W laser power and 800 mm/s scanning speed (c)

the pore is parallel to the scanning direction. This unusual phenomenon may be due to the fact that the powder is not fully melted in the longitudinal direction and voids are left. Fortunately, this kind of pore does not extend all the time, and after a few tracks, it stops expanding and accumulating due to

the flow of liquid metal. In contrast to the irregular defects with low energy, spherical defects formed with high energy (210 W, and 800 mm/s) are also characterized, as shown in Fig. 12(c). When the laser power is relatively high, the evaporation and vaporization of low melting point metal produce recoil pressure, and thus the depression is formed on the surface. If the subsequent liquid metal is not filled effectively, spherical defects are formed.

3.2.3 Multi-track multi-layer samples

The multi-track multi-layer experiments were carried out on Ti6Al4V samples according to the determined parameters (P=150 W, v=1600 mm/s; P=180 W, v=1200 mm/s; P=210 W, v=800 mm/s).

The morphology and pore characteristics of multi-track multi-layer Ti6Al4V samples via XCT with three processing parameters are illustrated in Fig. 13. Under the action of recoil pressure, the molten pool is unstable due to the wetting and Marangoni convection, resulting in a solidified layer with spheroidization and discontinuous shape. In the processing from 4-track 4-layer to 6-track 6-layer with a power of 150 W and scanning speed of 1600 mm/s, 4-track 4-layer can be considered as a consolidated layer. The formation of defects in 6-track 6-layer samples is attributed to the surface roughness of 4-track 4-layer, which determines the wettability of the molten pool. When the energy density is too low, which is not conducive to the diffusion of molten liquid materials and the effective filling of subsequent metal liquid pores, the width of the molten pool becomes narrow and the depth becomes shallow, and thus the melting

zone does not reach the bottom of the molten pool. As a result, the next layer of the molten track is difficult to cover the unmelted part of the previous layer. Once there are pores between the melting tracks, the LOF defects can be formed in the interior of the parts. According to the above analysis, it becomes evident that the surface roughness of the previously solidified layer and the energy density are important factors affecting the LOF defects of the new powder layer, which leads to stress concentration and seriously reduces the performance of the parts. By contrast, with a higher power of 210 W and a scanning speed of 800 mm/s, the molten pool can be fully wetted. The deep keyhole in the previous layer can be eliminated and new pores are generated because of disturbance between molten pools. The new pores are nearly spherical and randomly distributed.

Based on the above experimental results, it is necessary to make statistics on the porosity of different tracks and layers of Ti6Al4V samples, which can help to see the law of pore accumulation. Table 5 gives the porosity of Ti6Al4V samples with different tracks and layers at three processing parameters. When the energy density is low, with the increase of the number of tracks and layers, the porosity of the Ti6Al4V samples increases significantly and reaches 5.21% at 8-track 8-layer. However, at high energy density (P=180 W, v=1200 mm/s; P=210 W, v=800 mm/s), the overall trend of porosity of the Ti6Al4V samples increases at first and then decreases with the increase of tracks. This could be attributed to the fact that, in
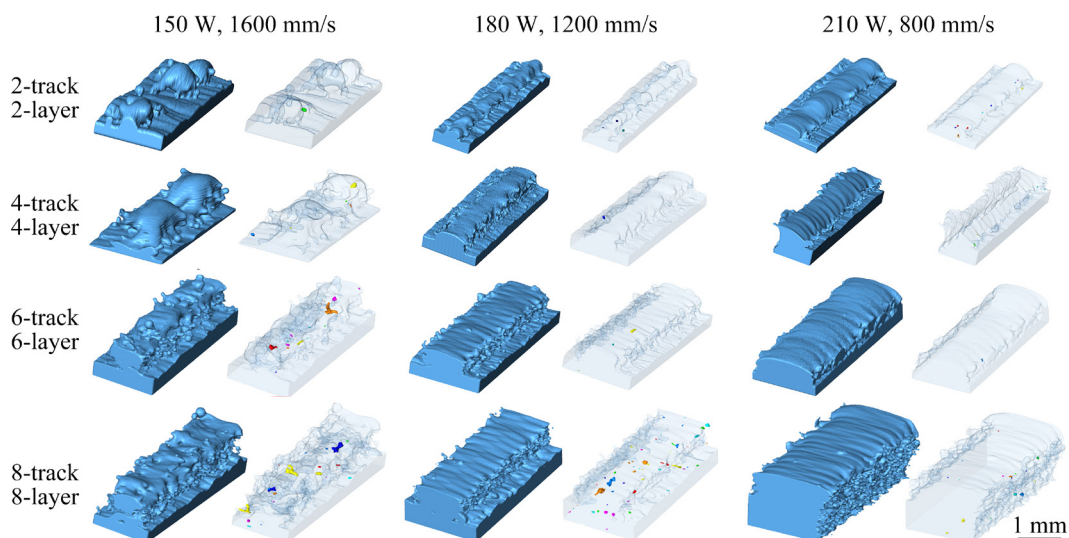

Fig. 13 Ti6Al4V samples morphology and pore characteristics with 2-track 2-layer, 4-tracks 4-layer, 6-track 6-layer, and 8-track 8-layer via XCT with three processing parameters

Table 5 Porosity of Ti6Al4V samples with different tracks and layers at three processing parameters

Number of tracks	Number of layers	Porosity/%		
		150 W, 1600 mm/s	180 W, 1200 mm/s	210 W, 800 mm/s
2	2	0.62	0.56	0.23
2	4	1.04	0.42	0.27
2	6	2.33	0.67	0.22
2	8	0.90	0.90	3.05
4	2	0.58	1.61	0.21
4	4	2.16	0.28	0.13
4	6	2.72	0.70	0.26
4	8	1.32	4.76	1.50
6	2	2.25	0.51	0.28
6	4	2.69	0.60	0.25
6	6	4.87	0.33	0.59
6	8	3.63	4.37	1.29
8	2	3.04	0.60	0.03
8	4	3.15	0.42	0.12
8	6	5.83	0.32	0.17
8	8	5.21	1.77	0.21

the first four tracks, since the laser is not completely stable, the molten pool might oscillate, and the porosity increases accordingly. As the laser stabilizes, the wetting of the molten metal is better, the overlap between the melt tracks tends to be smooth, the pores are partially melted, and the porosity decreases. When taking layers into consideration, when the energy is high, the increase of the number of layers does not mean that the porosity increases all the time. It is worth noting that the decrease of porosity is attributed to the decrease of pore volume and the change of macropores into small pores, instead of a decrease in number.

Through the 3D characterization of the morphology and defects of the multi-track multi-layer molten pool, it is concluded that the surface roughness of the former layer can greatly affect the melting quality of the next layer, and the pores occur between the layers or accumulate to the next layer. The wetting behavior between the powder and the substrate plays an important role in eliminating the interlayer LOF defects. Moreover,

low energy density may not be sufficient to melt the underlying substrate, but inhibits wetting behavior and leads to the formation of interlayer defects. Properly increasing the solidification time and reducing the scanning speed can help to ensure the wetting quality and increase the stability of the deposition melting pool.

4 Conclusions

(1) The processing window of SLM Ti6Al4V defects is classified based on three types: keyhole defects zone, optimal parameters zone and LOF defects zone. Most of the pores are perpendicular to the construction direction and the curvature of the defect varies with different laser powers and scanning speeds.

(2) According to the sphericity, the defects of SLM TiAl4V bulk samples with different processing parameters are classified into four categories: spherical (0.9−1), elliptical-shaped (0.7−0.9), elongated-shaped (0.4−0.7), and irregularly-shape (0−0.4), and their proportion in the block is calculated. The elliptical- and elongated-shaped defects account for a large proportion of defects in most bulk samples, followed by spherical and irregularly-shaped.

(3) The quantitative and qualitative characterization of the defects of track-by-track and layer-by-layer is analyzed. It is found that reasonable processing parameters can ensure the stability of the melting pool, and porosity can gradually accumulate with the overlay of layers. The volume and number of LOF defects increase at low power with the increase of tracks. However, with excessive power, as a new track is formed, the pores between the tracks in the upper layer may disappear.

Acknowledgments

References

[1] HERZOG D, SEYDA V, WYCISK E, EMMELMANN C. Additive manufacturing of metals [J]. Acta Materialia, 2016, 117: 371−392.

[2] YAN La-mei, YU Jiang-hong, ZHONG Yu-xing, GU Yan, MA Yu-peng, LI Wen-xin, YAN Jia, GE Yun-yang, YIN Jun-hui, LUO Yun-xiao, MIRZASADEGHI A, YUAN You-wei. Influence of scanning on nano crystalline β-Ti alloys fabricated by selective laser melting and their applications in biomedical science [J]. Nanoscience and Nanotechnology, 2020, 20(8): 1605−1612.

[3] LIU Xin-yu, PAN Lu, WANG Wen-hao, LI Si-yao. Experimental study on pore-defect by selective laser melting of 316L stainless steel [J]. Key Engineering Materials, 2019, 801: 239−244.

[4] ALI H, GHADBEIGI H, MUMTAZ K. Effect of scanning strategies on residual stress and mechanical properties of selective laser melted Ti6Al4V [J]. Materials Science and Engineering A, 2018, 712: 175−187.

[5] ALI H, GHADBEIGI H, MUMTAZ K. Processing parameter effects on residual stress and mechanical properties of selective laser melted Ti6Al4V [J]. Journal of Materials Engineering and Performance, 2018, 27(8): 4059−4068.

[6] LAURSEN C M, DEJONG S A, DICKENS S, EXIL A N, SUSAN D F, CARROLL J D. Relationship between ductility and the porosity of additively manufactured AlSi10Mg [J]. Materials Science and Engineering A, 2020, 795: 139922.

[7] GLODEŽ S, KLEMENC J, ZUPANIČ F, VESENJAK M. High-cycle fatigue and fracture behaviours of SLM AlSi10Mg alloy [J]. Transactions of Nonferrous Metals Society of China, 2020, 30(10): 2577−2589.

[8] NEIKTER M, FORSBERG F, PEDERSON R, ANTTI M L, ÅKERFELDT P, LARSSON S, JONSEN P, PUYOO G. Defect characterization of electron beam melted Ti−6Al−4V and Alloy 718 with X-ray microtomography [J]. Aeronautics and Aerospace Open Access Journal, 2018, 2(3): 139−145.

[9] SNOW Z, NASSAR A R, REUTZEL E W. Review of the formation and impact of flaws in powder bed fusion additive manufacturing [J]. Additive Manufacturing, 2020, 36: 101457.

[10] YANG Jing-jing, HAN Jie, YU Han-chen, YIN Jie, GAO Ming, WANG Ze-min, ZENG Xiao-yan. Role of molten pool mode on formability, microstructure and mechanical properties of selective laser melted Ti−6Al−4V alloy [J]. Materials & Design, 2016, 110: 558−570.

[11] SHRESTHA Su-bin, CHOU K. Build location effect on the single-track pore characteristics formed with the laser powder bed fusion process [J]. Manufacturing Letters, 2021, 28: 6−10.

[12] SIDDIQUE S, IMRAN M, RAUER M, KALOUDIS M, WYCISK E, EMMELMANN C, WALTHER F. Computed tomography for characterization of fatigue performance of selective laser melted parts [J]. Materials & Design, 2015, 83: 661−669.

[13] ZHOU X, DAI N, CHENG X S, THOMPSON A, LEACH R. Three-dimensional characterization of powder particles using X-ray computed tomography [J]. Additive Manufacturing, 2021, 40: 101913.

[14] YAO Xin-xin, LI Jian-yu, WANG Yi-fei, GAO Xiang, ZHANG Zhao. Numerical simulation of powder effect on solidification in directed energy deposition additive manufacturing [J]. Transactions of Nonferrous Metals Society of China, 2021, 31(9): 2871−2884.

[15] WALKER K F, LIU Q, BRANDT M. Evaluation of fatigue crack propagation behaviour in Ti−6Al−4V manufactured by selective laser melting [J]. International Journal of Fatigue, 2017, 104: 302−308.

[16] ZHANG Bi, LI Yong-tao, BAI Qian. Defect formation mechanisms in selective laser melting: A review [J]. Chinese Journal of Mechanical Engineering, 2017, 30(3): 515−527.

[17] SHIPLEY H, MCDONNELL D, CULLETON M, COULL R, LUPOI R, DONNELL O, TRIMBLE D. Optimisation of process parameters to address fundamental challenges during selective laser melting of Ti−6Al−4V: A review [J]. International Journal of Machine Tools and Manufacture, 2018, 128: 1−20.

[18] JIANG Xi-yi, XIA Wei-long, LOU Dian-jun, REN Xue-peng, SHAO Shuai, LI Hao-qing, LIU Shu-yu, FANG Xiao-ying. Effect of scanning speed on internal defects and mechanical properties of Ti−6Al−4V alloy processed by selective laser melting [J]. Materials for Machanical Engineering, 2020, 44(11): 41−45.

[19] LIU Wei, CHEN Chao-yue, SHUAI San-san, ZHAO Rui-xin, LIU Long-tao, WANG Xiao-dong, HU Tao, XUAN Wei-dong, LI Chuan-jun, YU Jian-bo, WANG Jiang, REN Zhong-ming. Study of pore defect and mechanical properties in selective laser melted Ti6Al4V alloy based on X-ray computed tomography [J]. Materials Science and Engineering A, 2020, 797: 139981.

[20] HU Y N, WU S C, WITHERS P J, ZHANG J, BAO H Y X, FU Y N, KANG G Z. The effect of manufacturing defects on the fatigue life of selective laser melted Ti−6Al−4V structures [J]. Materials & Design, 2020, 192: 108708.

[21] ZEKAVAT A R, JANSSON A, LARSSON J, PEJRYD L. Investigating the effect of fabrication temperature on mechanical properties of fused deposition modeling parts using X-ray computed tomography [J]. The International Journal of Advanced Manufacturing Technology, 2018, 100(1/2/3/4): 287−296.

[22] LIU Tian-yu, MIN Xiao-hua, ZHANG Shuang, WANG Cun-shan, DONG Chuang. Microstructures and mechanical properties of Ti−Al−V−Nb alloys with cluster formula manufactured by laser additive manufacturing [J]. Transactions of Nonferrous Metals Society of China, 2021, 31(10): 3012−3023.

[23] SHUTOV I V, GORDEEV G A, KHARANZHEVSKIY E V, KRIVILYOV M. D. Analysis of morphology and residual porosity in selective laser melting of Fe powders using single track experiments [J]. IOP Conference Series: Materials Science and Engineering, 2017, 192: 012023.

[24] DU PLESSIS A, YADROITSEV I, YADROITSAVA I, LE ROUX S G. X-Ray Microcomputed tomography in additive manufacturing: A review of the current technology and applications [J]. 3D Printing and Additive Manufacturing, 2018, 5(3): 227−247.

[25] CHEN Yao, PENG Xing, KONG Ling-bao, DONG Guang-xi, REMANI A, LEACH R. Defect inspection technologies for additive manufacturing [J]. International Journal of Extreme Manufacturing, 2021, 3(2): 022002.

[26] ROMANO S, ABEL A, GUMPINGER J, BRANDÃO A D, BERETTA S. Quality control of AlSi10Mg produced by SLM: Metallography versus CT scans for critical defect size assessment [J]. Additive Manufacturing, 2019, 28: 394−405.

[27] WU Shi-biao, DOU Wen-hao, TANG Yong-qiang, WANG Di, CHEN Xiao-jun, LIANG Yi-fu. Research progress of inspection technology for addition manufacturing of SLM Metal [J]. Journal of Netshape Forming Engineering, 2019, 11(4): 37−49.

[28] ELAMBASSERIL J, LU S L, NING Y P, LIU N, WANG J, BRANDT M, TANG H P, QIAN M. 3D characterization of defects in deep-powder-bed manufactured Ti−6Al−4V and their influence on tensile properties [J]. Materials Science and Engineering A, 2019, 761: 138031.

[29] SANAEI N, FATEMI A, PHAN N. Defect characteristics and analysis of their variability in metal L-PBF additive manufacturing [J]. Materials & Design, 2019, 182: 108091.

[30] STEF J, POULON-QUINTIN A, REDJAIMIA A, GHANBAJA J, FERRY O, SOUSA M D, GOUNE M. Mechanism of porosity formation and influence on mechanical properties in selective laser melting of Ti−6Al−4V parts [J]. Materials & Design, 2018, 156: 480−493.

[31] NIE Xiao-jia, ZHANG Hu, ZHU Hai-hong, HU Zhi-heng, KE Lin-da, ZENG Xiao-yan. Analysis of processing parameters and characteristics of selective laser melted high strength Al−Cu−Mg alloys: From single tracks to cubic samples [J]. Journal of Materials Processing Technology, 2018, 256: 69−77.

[32] TANG C, TAN J L, WONG C H. A numerical investigation on the physical mechanisms of single track defects in selective laser melting [J]. International Journal of Heat and Mass Transfer, 2018, 126: 957−968.

[33] XIANG Yu, ZHANG Shu-zhe, WEI Zheng-ying, LI Jun-feng, WEI Pei, CHEN Zhen, YANG Li-xiang, JIANG Li-hao. Forming and defect analysis for single track scanning in selective laser melting of Ti6Al4V [J]. Applied Physics A, 2018, 124(10): 685.

[34] SHRESTHA S, STARR T, CHOU K. A study of keyhole porosity in selective laser melting: Single-track scanning with micro-CT analysis [J]. Journal of Manufacturing Science and Engineering, 2019, 141(7): 071104.

[35] MISHUROVA T, ARTZT K, HAUBRICH J, REQUENA G, BRUNO G. New aspects about the search for the most relevant parameters optimizing SLM materials [J]. Additive Manufacturing, 2019, 25: 325−334.

[36] XIAO Ling, LU Ming-yuan, HUANG Han. Detection of powder bed defects in selective laser sintering using convolutional neural network [J]. International Journal of Advanced Manufacturing Technology, 2020, 107(5/6): 2485−2496.

[37] CAI Xing-fang, MALCOLM A A, WONG B S, FAN Z. Measurement and characterization of porosity in aluminium selective laser melting parts using X-ray CT [J]. Virtual and Physical Prototyping, 2015, 10(4): 195−206.

[38] SCIPIONI BERTOLI U, WOLFER A J, MATTHEWS M J, DELPLANQUE J R, SCHOENUNG J M. On the limitations of volumetric energy density as a design parameter for selective laser melting [J]. Materials & Design, 2017, 113: 331−340.

[39] SALARIAN M, ASGARI H, VLASEA M. Pore space characteristics and corresponding effect on tensile properties of Inconel 625 fabricated via laser powder bed fusion [J]. Materials Science and Engineering A, 2020, 769: 138525.

[40] HU Y N, WU S C, WU Z K, ZHONG X L, AHMED S, KARABAL S, XIAO X H, ZHANG H O. A new approach to correlate the defect population with the fatigue life of selective laser melted Ti−6Al−4V alloy [J]. International Journal of Fatigue, 2020, 136: 105584.

[41] PUNCREOBUTR C, LEE P D, KAREH K M, CONNOLLEY T, FIFE J L, PHILLION A B. Influence of Fe-rich intermetallics on solidification defects in Al−Si−Cu alloys [J]. Acta Materialia, 2014, 68: 42−51.

[42] PROMOPPATUM P, YAO S C. Influence of scanning length and energy input on residual stress reduction in metal additive manufacturing: Numerical and experimental studies [J]. Journal of Manufacturing Processes, 2020, 49: 247−259.

[43] FELBERBAUM M, RAPPAZ M. Curvature of micropores in Al−Cu alloys: An X-ray tomography study [J]. Acta Materialia, 2011, 59: 6849−6860.

[44] SNELL R, TAMMAS-WILLIAMS S, CHECHIK L, LYLE A, HERNÁNDEZ-NAVA E, BOIG C, PANOUTSOS G, TODD I. Methods for rapid pore classification in metal additive manufacturing [J]. JOM, 2019, 72: 101−109.

[45] HASTIE J C, KARTAL M E, CARTER L N, ATTALLAH M M, MULVIHILL D M. Classifying shape of internal pores within AlSi10Mg alloy manufactured by laser powder bed fusion using 3D X-ray micro computed tomography: Influence of processing parameters and heat treatment [J]. Materials Characterization, 2020, 163: 110225.

[46] ZHU Yun-hui, WU Zi-ling, HARTLEY W D, SIETINS J M, WILLIAMS C B, YU H Z. Unraveling pore evolution in post-processing of binder jetting materials: X-ray computed tomography, computer vision, and machine learning [J]. Additive Manufacturing, 2020, 34: 101183.

[47] HUSSAIN M, GUPTA P, KUMAR P, DAS A K. Selective laser melting of single track on Ti−6Al−4V powder: Experimentation and finite element analysis [J]. Arabian Journal for Science and Engineering, 2020, 45(2): 1173−1180.

[48] MARTIN A A, CALTA N P, KHAIRALLAH S A, WANG J, J DEPOND P, FONG A Y, THAMPY V, GUSS G M, KISS A M, STONE K H, TASSONE C J, WEKER J N, TONEY M F, BUUREN T V, MATTHEWS M J. Dynamics of pore formation during laser powder bed fusion additive manufacturing [J]. Nature Communications, 2019, 10(1): 1987.

[49] JING Guan-yi, WANG Ze-min. Defects, densification mechanism and mechanical properties of 300M steel deposited by high power selective laser melting [J]. Additive Manufacturing, 2021, 38: 101831.

[50] BAITIMEROV R M. Single track formation during selective laser melting of Ti−6Al−4V alloy [J]. Materials Science Forum, 2019, 946: 978−983.

利用微计算机断层扫描定量研究选择性激光熔化 Ti6Al4V 合金缺陷的几何特征及形成机理

安娜莹[1]，帅三三[1]，陈超越[1]，雷力明[2]，王 江[1]，任忠鸣[1]

1. 上海大学 材料科学与工程学院 省部共建高品质特殊钢冶金与制备国家重点实验室，上海 200444；
2. 中国航发上海商用飞机发动机制造有限公司，上海 201306

摘 要： 增材制造(AM)部件内部形成的缺陷对打印零件的力学性能具有不利影响。缺陷对零件性能的影响因其几何特征的不同而不同。利用 X 射线计算机层析成像(XCT)研究不同打印参数下 36 个块状 Ti6Al4V 样品的孔隙缺陷特征。根据样品中孔隙的几何特征，将孔隙缺陷分为 4 种类型：球形、椭圆形、长条形和不规则形。在所有工艺参数下，长条形状缺陷所占比例最大，并且随着扫描速度的提高，不规则形状缺陷所占比例逐渐增大。另外，分析单道和多道试样中缺陷逐渐积累规律。随着层的叠加，孔隙逐渐积累，而适当的搭接率可能会熔化道之间的气孔。表面粗糙度和熔池润湿对缺陷的形成有很大的影响。

关键词： 选择性激光熔化；X 射线计算机断层扫描；气孔缺陷；3D 几何形态；形成机制；Ti6Al4V 合金

(Edited by Bing YANG)